



Photoelastic and numerical investigation of stress distributions around fault models under biaxial compressive loading conditions

Ghislain de Jossineau^{a,*}, Jean-Pierre Petit^a, Bertrand D.M. Gauthier^b

^a*Laboratoire de Géophysique, Tectonique et Sédimentologie (UMR 5573), c.c 060, Université Montpellier II, Place Eugène Bataillon, 34095 Montpellier, cedex 5, France*

^b*TotalFinaElf, DGEP/TG/CEG/CMR, 2 place de la Coupole, La Défense 6, 92078 Paris La Défense, France*

Received 25 February 2002; accepted 8 November 2002

Abstract

This paper presents the results of a photoelastic and numerical study of stress distributions (contours and trajectories) around fault models of various geometries, submitted to a biaxial compressive load. It aims to describe typical biaxial stress behaviours and emphasize the existing differences with the well-known uniaxial compressive load case. Stress trajectories are sometimes shown by joint sets acting as markers of a paleostress field, and they can be interpreted by particular shallow tension–compression situations. At depth fractures can be reactivated, or can dilate under conditions of triaxial compression, and behaviour is essentially controlled by a high stress ratio (high σ_3/σ_1 ratio). In spite of the potential importance of such stress states on fracture permeability and fluid flow, and although they are frequently found at depth in a reservoir context, such stress conditions are poorly investigated, particularly in terms of stress perturbations.

The presented analogue experiments consisted of compression tests done on polymethylmethacrylate (PMMA) plates; this material has mechanical properties comparable to those of brittle rocks in the upper crust, and presents birefringence. The samples contained open defects acting as faults, and the stress trajectories around these faults were investigated using a photoelastic device. Comparable numerical experiments were realised with a finite-element code (Franc 2D), using frictionless fault models.

First, the effect of an increasing biaxial compressive load ratio σ_3/σ_1 on stress trajectories around an isolated open defect was explored. It was shown that the stress trajectories were drastically modified when σ_3/σ_1 increased from 0.2 to 0.4, this result being consistent with previous studies. In particular, when σ_3/σ_1 was superior or equal to 0.4, external isotropic points around where trajectories diverged (called repulsive isotropic points) appeared near the tips, but away from the defects. They tended to move away from the defects towards the main load direction when σ_3/σ_1 increased. The described isotropic points were points of stress trajectory divergence, i.e. points where stress decreased, implying that zones around them were strongly unfavourable to shear reactivation.

Second, stress trajectories around fault models of various geometries (oblique isolated defect, dilational jog, compressive jog, and complex patterns) were studied, the applied biaxial compressive load ratio being 0.7. These biaxial stress trajectories were compared with similar uniaxial stress trajectories in order to explore the existing differences between the two regimes. It enabled new stress trajectory geometries to be described and interpreted. In particular, numerous external repulsive isotropic points were observed, and defect tips were shown to be zones of high convergence of stress trajectories. Furthermore, in contrast

* Corresponding author.

E-mail address: ghislain.de.jossineau@dstu.univ-montp2.fr (G. de Jossineau).

to the uniaxial compressive load case, stress trajectories and stress contours were geometrically similar within dilational and compressive jogs under biaxial compressive load. For both jog types, the centre of the overlapping zone, and the areas along the wall of a jog-defining fault and facing the overlapping tip of the other fault, proved to be zones of low mean stress, implying that fluids may migrate towards them from the tips of the faults, in response to mean stress gradients. Furthermore, the centre of the jogs exhibiting a high differential stress was a favourable area in terms of fracture reactivation, which may facilitate fluids transfer and storage.

It was also observed that for both the uniaxial and biaxial compressive loads, isotropic zones were localised at the acute angle between branching defects.

© 2002 Elsevier Science B.V. All rights reserved.

Keywords: Biaxial compressive load; Stress trajectories; Stress contours; Photoelasticity; Isotropic points and zones; Fluid flow

1. Introduction

In the earth's crust, and particularly in basin contexts, in situ stress regimes generally show horizontal stress ratios σ_h/σ_H , often above 0.5 which can even reach 1 at depth (see σ_h and σ_H measurements from Zoback et al., 1980; Haimson and Rummel, 1982; Haimson and Doe, 1983; Stock and Healy, 1988; Baumgärtner and Zoback, 1989; Evans et al., 1989 compiled in Engelder, 1993). Such biaxial stress regimes are expected to be influential on aperture and/or reactivation of fractures (particularly shear reactivation), and then may indirectly have important consequences on fracture permeability and fluid flow: indeed, shear reactivation of fractures may locally increase their permeability and more generally favour connectivity between pre-existing and newly formed fracture sets (Brown, 1987; Dholakia et al., 1998; Taylor et al., 1999).

Numerical studies of perturbed stress field around faults generally take into account unrealistic boundary conditions such as two horizontal tensile stresses in extensional regime (Kattenhorn et al., 2000; Kattenhorn and Pollard, 2001), or biaxial extension (Maerten et al., 2002), or specify unrealistic modelling parameters as plane stress conditions (Bertoluzza and Perotti, 1997). Experimental studies devoted to the influence of stress on fluid flow around dilational jogs are done under simple shear loading (Connolly and Cosgrove, 1999a,b), and the same condition is imposed by Bourne et al. (2001) who aim at predicting complex stress fields, and hence, fracture and flow around frictionless fault patterns. These studies have provided useful data and explored many aspects of fracturing related to faulting. Indeed, uniaxial compressive or

tensile compressive loading conditions help to explain stress trajectories sometimes exhibited by joints (mode I fractures) acting as markers of σ_H paleostress field trajectories in non-perturbed domains (Engelder and Geiser, 1980), or perturbed domains next to faults (Rawnsley et al., 1992, 1997; Auzias et al., 1997).

However, these loading conditions do not take into account the reality of biaxial compressive stress conditions, which are not currently known to modify the stress field drastically. Very few works aiming to describe stress distributions around fault patterns consider biaxial compressive loading conditions. Among them, the study by Segall and Pollard (1980) investigated the state of stress near echelon discontinuities under moderate biaxial compressive loading conditions ($\sigma_3/\sigma_1=0.2$), and predicted the secondary fracturing associated with such stress distributions, but without studying stress trajectories. In fact, only a very small number of studies demonstrate the change in stress trajectories related to change in biaxial compressive stress ratio. This is suggested in Fig. 9b in Barquins and Petit (1992) and in Fig. I.II.10b in Auzias (1995). To our knowledge, no description of the evolution of stress trajectories around fault patterns with changing biaxial compressive stress ratio is available.

Several fundamental questions need an answer:

- What are the stress trajectories around a fault submitted to a strong biaxial stress ratio?
- Is there a threshold value of the biaxial compressive load ratio (σ_3/σ_1) for which the distribution of stress trajectories is drastically changed?
- What is the effect of biaxial compressive load on stress trajectories in dilational and compressive

jogs, and what are the differences with the uniaxial compressive load case?

- What are the stress (σ_1 and σ_3) distributions (contours and trajectories) within and around dilational and compressive jogs under biaxial compressive load, and what are the possible hydrodynamical implications of such stress fields (fracture reactivation, fluid flow...)?

In this paper, we present the results of a study coupling photoelastic and numerical modelling, which aims to investigate the questions above. We chose the photoelasticity method because it is very well adapted to the detailed analysis of stress within models. It has widely been used in physics of materials to determine stress parameters like stress intensity factors at the tips of cracks (Barker et al., 1985; Dally and Sanford, 1978, 1987; Feng et al., 1991; Sanford, 1989) and has successfully been adapted to more geological goals such as the determination of stress state close to rock joints (Hyett and Hudson, 1990) and the determination of stress trajectories around complex defects patterns (Auzias, 1995; Auzias et al., 1997). In the present study, we tested first the influence of an increasing biaxial compressive load ratio on stress trajectories around a simple open fault model, and secondly, the effect of large biaxial compressive load ratio on stress trajectories and stress distributions within and around jog zones, the obtained stress trajectories being compared with similar trajectories under uniaxial compressive load. These simple situations were explored with the idea of modelling more complex fault patterns inspired from petroleum application.

In both analogue and numerical experiments, the fault models were frictionless defects of various geometries in order to compare the results with most of the numerical works done with frictionless faults (Connolly and Cosgrove, 1999a,b; Bourne et al., 2001; Bourne and Willemsse, 2001; Bertoluzza and Perotti, 1997). The effects of friction will be investigated separately.

In the analogue experiments, the defects were cut in polymethylmethacrylate (PMMA) plates, because this material is birefringent so that the photoelastic method of stress analysis can be used (Auzias et al., 1997). Furthermore, it has a well-known mechanical behaviour which can be compared, in laboratory

conditions, to that of upper crust brittle rocks. This material has widely been used as a rock analogue in rupture mechanics experiments (Nemat-Nasser and Horii, 1982; Petit and Barquins, 1987; Barquins and Petit, 1992) and in friction experiments (Wu et al., 1972; Dieterich and Kilgore, 1994, 1996; Bouissou et al., 1998a,b,c; Bodin et al., 1998; de Joussineau et al., 2001).

2. Photoelastic method of stress trajectory determination

Photoelasticity is an optical method of stress analysis within materials like PMMA which present accidental birefringence when loaded, their optical properties being modified in function of the intensity of applied deformation. These materials have the property of resolving the light which falls on them at normal incidence into two components, each one coinciding with a principal plane of stress within the sample, and of transmitting them at right angles (Hetényi, 1966). If a photoelastic sample is placed between polarizers whose axes are perpendicular (crossed polarizers), black fringes named isoclinics appear in the sample when the plane of the incident polarized light coincides with one direction of principal stress within the sample. These isoclinics move when the polarizers rotate together. By rotating the polarizers from 0° to 90° , and drawing the corresponding isoclinics, it is possible to determine point to point the orientation of the two principal stresses in a model, and then to trace the stress trajectories. In the following, the represented stress trajectories are those of the local major principal stress (σ_{1L} local).

A second photoelastic pattern corresponds to isochromatics, which are coloured lobes of isovalue of differential stress, and are not used here. They are superposed on isoclinics and may perturb their observation, so they were avoided simply by applying a low level of stress to the samples.

The photoelastic method of stress trajectory reconstruction is as follows. During a photoelastic experiment, the studied samples are tested between two crossed polarizers which can rotate simultaneously: this device permits the isoclinics to be observed within the samples at various orientations of the polarizers. A photoelastic device is shown in Fig. 1.

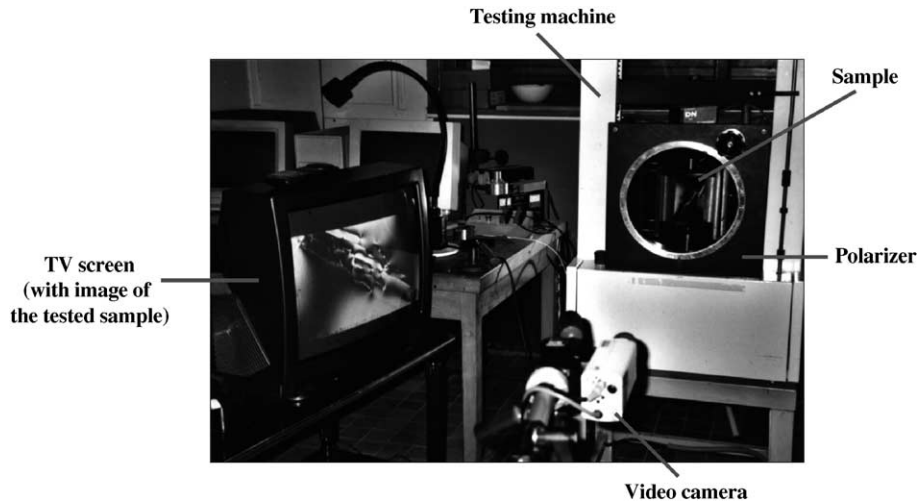


Fig. 1. Photograph of a photoelastic experiment, showing the tested sample placed between crossed polarizers.

To determine the stress trajectories within a test sample, the experiments are recorded using a video camera, and isoclinics are then traced from television

images. A 10° (or less if necessary) rotation of the polarizers separates each observation of isoclinics. Along each observed isoclinic (Fig. 2a), crosses

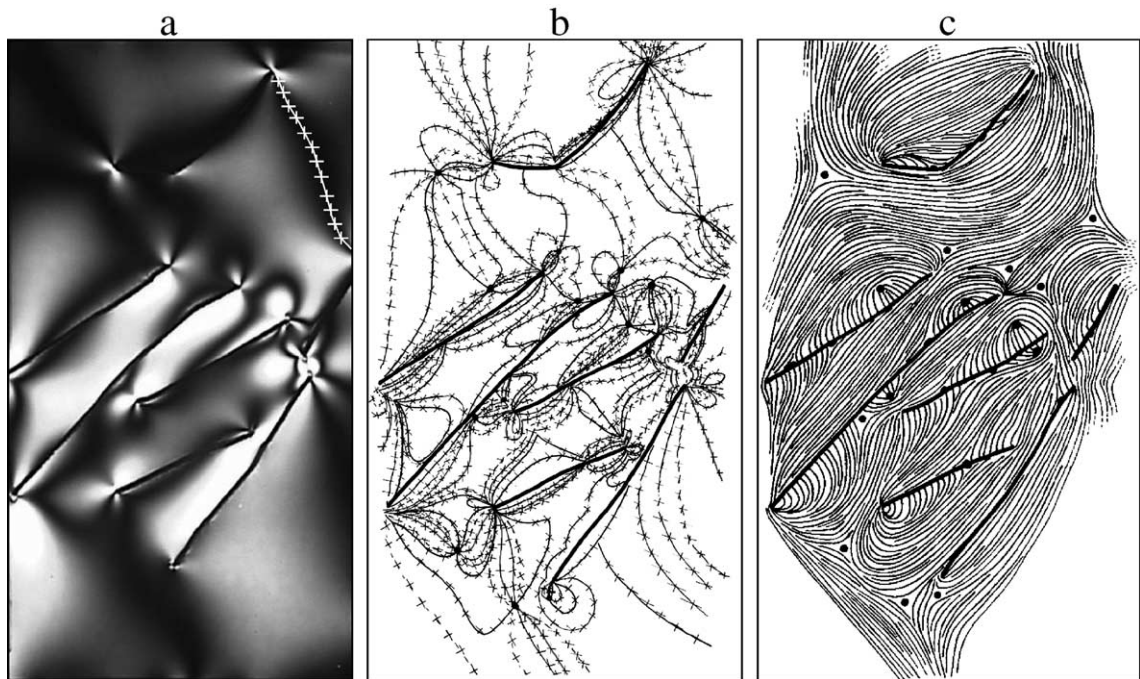


Fig. 2. Photoelastic method of stress trajectory reconstitution within a sample. (a) Photograph of a photoelastic experiment showing isoclinics 0° around complex fault patterns under biaxial compressive load (one isoclinic is underlined). (b) Crosses representing the orientations of the two principal stresses within the sample are drawn on each observed isoclinics. (c) σ_{1L} trajectories, indicated by the crosses, are traced point to point within the sample (black points on the figure are isotropic points). More details in the text.

representing the respective orientations of the two principal stresses within the sample are then drawn (Fig. 2b). Orientations of polarizers from 0° to 90° are investigated, and stress trajectories, indicated by the crosses, are finally drawn point to point (Fig. 2c): spacing between them is arbitrarily chosen to permit the best legibility. Points or zones where stresses are equal (i.e. $\sigma_D = 0$, where σ_D is the differential stress) appear black during the polarizers' rotation. They are named isotropic points or zones meaning that no stress trajectories are present.

3. Experimental procedure

3.1. Analogue experiments

The analogue experiments consisted in biaxial compression tests of PMMA plates with dimensions of $200 \times 160 \times 6 \text{ mm}^3$, containing open defects of various size and geometry acting as pre-existing faults. In order to insert the fault related open defects within a plate, we drilled holes of 0.5 mm diameter along the path of the future defect, from which we cut the plates using a 0.3-mm-diameter micro-saw. Thus, open defects of well-controlled geometry were obtained (Fig. 3).

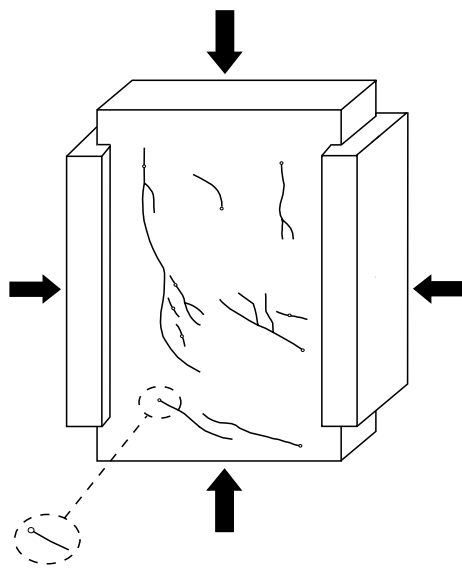


Fig. 3. Schematic cartoon of a PMMA sample containing several open fault models and its loading conditions.

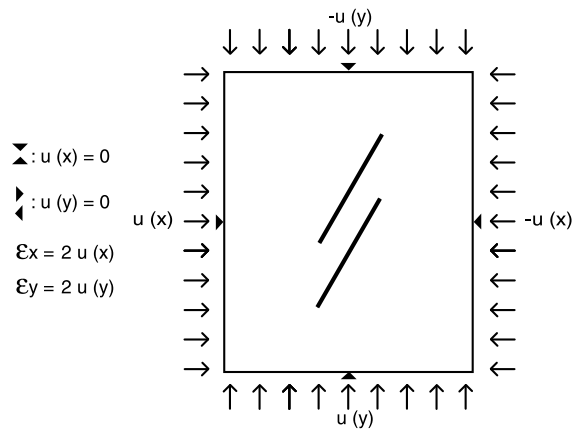


Fig. 4. Boundary conditions used in the numerical models.

The main compressive load was imposed by an electromechanic testing machine (Davenport 30 kN), and the lateral pressure was added by a hydraulic jack, the samples being maintained between vertical tighteners to prevent bending effects. The samples were tested using a photoelastic device shown in Fig. 1 and the stress trajectories around the fault models were analysed following the procedure shown in Fig. 2.

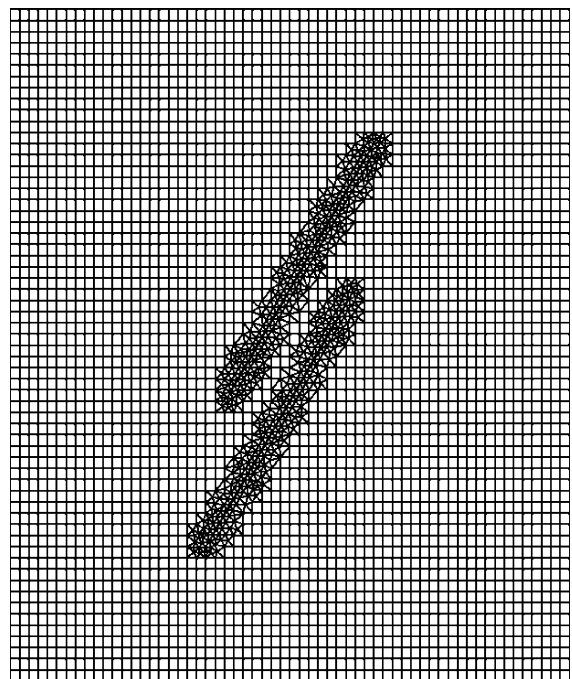


Fig. 5. FEM mesh of the model of dilational jog.

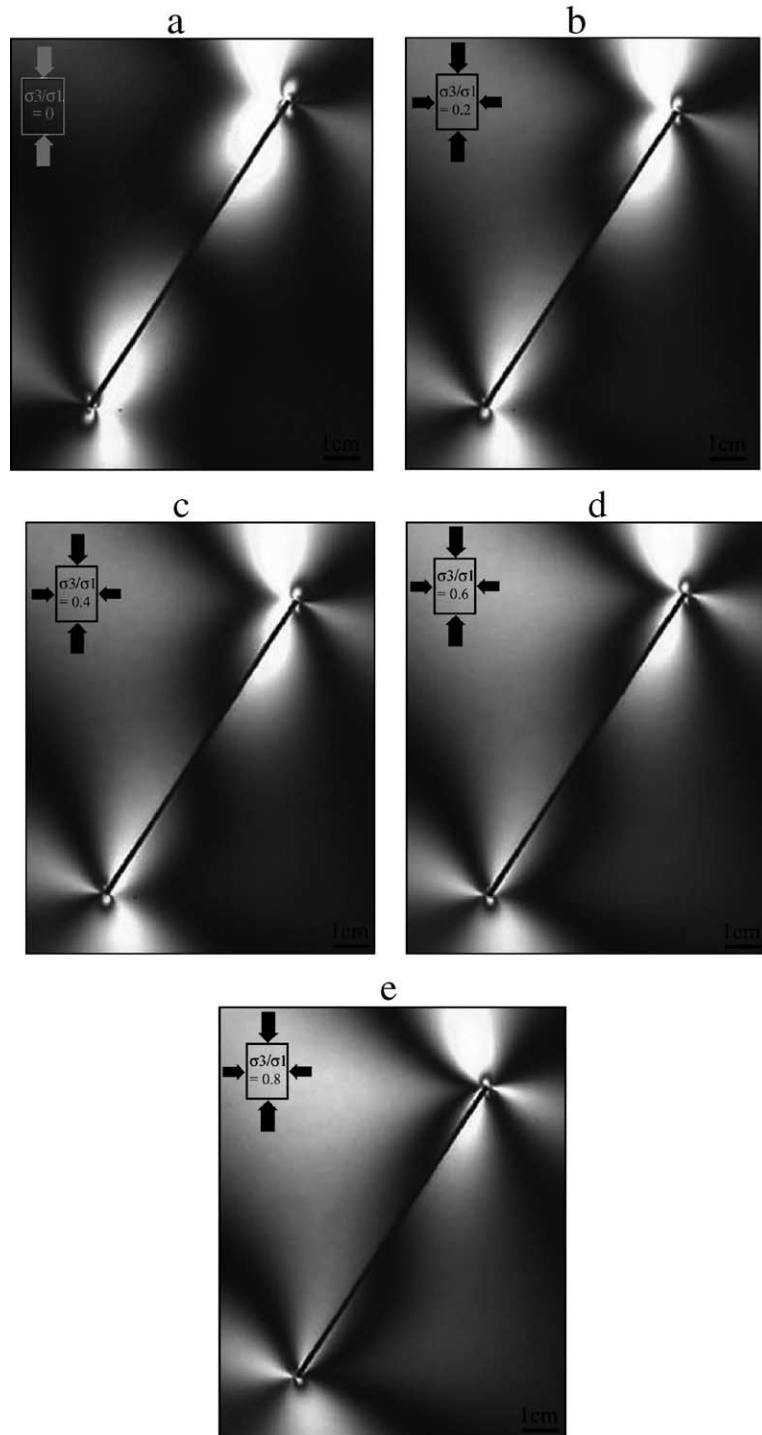


Fig. 6. Photograph of isoclinics 0° around an oblique isolated fault during a photoelastic experiment: (a) σ_3/σ_1 is 0; (b) σ_3/σ_1 is 0.2; (c) σ_3/σ_1 is 0.4; (d) σ_3/σ_1 is 0.6; (e) σ_3/σ_1 is 0.8.

A first set of experiments consisted in biaxial compression tests of an isolated oblique defect model. Its orientation was fixed at 30° to the vertical main load direction because this is the preferential sliding orientation in terms of displacement along the defect (de Jossineau et al., 2001). The effect of the biaxial compressive load ratio σ_3/σ_1 on stress trajectories was

tested by applying to the same sample a σ_3/σ_1 ratio ranging from 0 to 0.8.

Secondly, the effect of biaxial compressive load on stress trajectories around various fault models (isolated fault, dilational jog, compressive jog, and complex patterns) was studied, the applied biaxial compressive load ratio being 0.7 (this value was

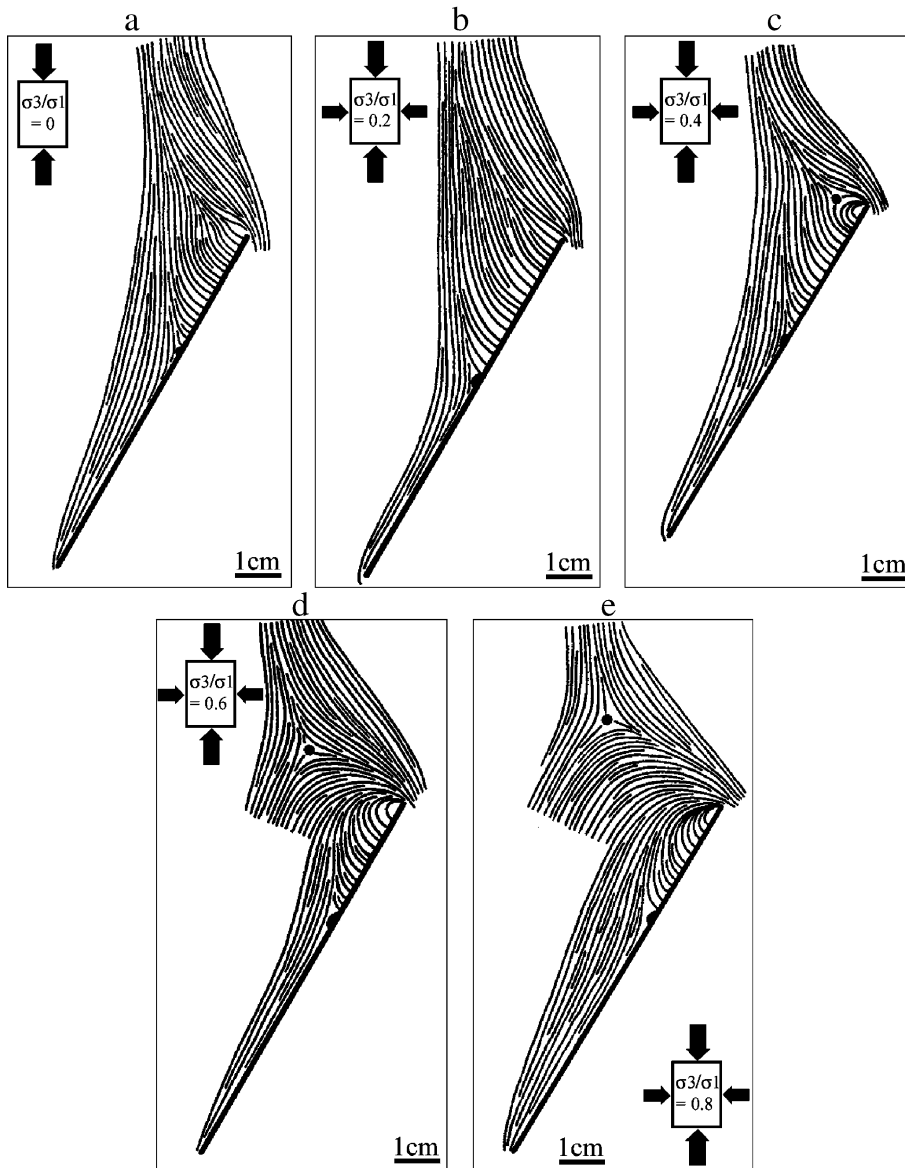


Fig. 7. σ_{1L} trajectories around an oblique isolated fault: (a) σ_3/σ_1 is 0; (b) σ_3/σ_1 is 0.2; (c) σ_3/σ_1 is 0.4; (d) σ_3/σ_1 is 0.6; (e) σ_3/σ_1 is 0.8. Note that for symmetry reasons, only half of the fault is shown here.

inspired from a field example). The same experiments were also done under uniaxial compressive load to compare with the biaxial compressive load case.

In the experiments, the orientation of overlapping defects was 30° with the vertical direction, and the jog zones were 2.5 times as large as the spacing between the faults.

3.2. Numerical experiments

The numerical experiments were realised using a finite-element code named Franc2D (Wawrzynek and

Ingraffea, 1987). The jog models were formed by non-cohesive cracks, and were geometrically identical with those used in the analogue experiments. The plates containing the cracks had characteristics similar to those of PMMA (elastic behaviour, Young modulus $E=3$ GPa and Poisson modulus $\nu=0.4$), and were tested under biaxial compressive load, using a plane strain condition. The boundary conditions of the numerical models are shown by Fig. 4. The main applied strain was the vertical strain ε_y , which was fixed to $0.001H$, H being the height of the models. The horizontal applied strain ε_x was calibrated in such a way that the ratio between the

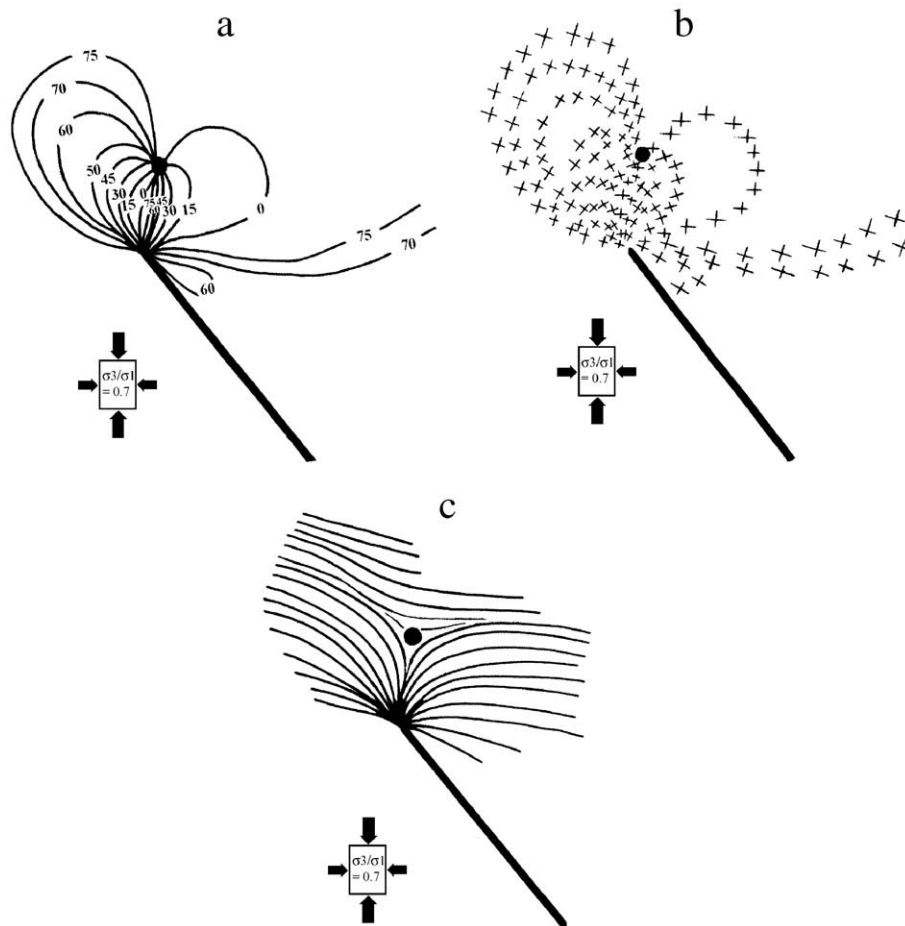


Fig. 8. Isoclinics (a), stress orientations (b) and σ_{1L} trajectories (c) corresponding to an external isotropic point close to a defect tip. The numbers on the isoclinics indicate the angle of polarizers with the vertical direction, and consequently, the orientation of one principal stress within the sample.

equivalent vertical (σ_1) and horizontal (σ_3) applied stress was equal to 0.7. These strains were comparable to the strains applied in the analogue experi-

ments. Fig. 5 shows the FEM mesh in the case of the dilational jog (the densest mesh is centred on the cracks).

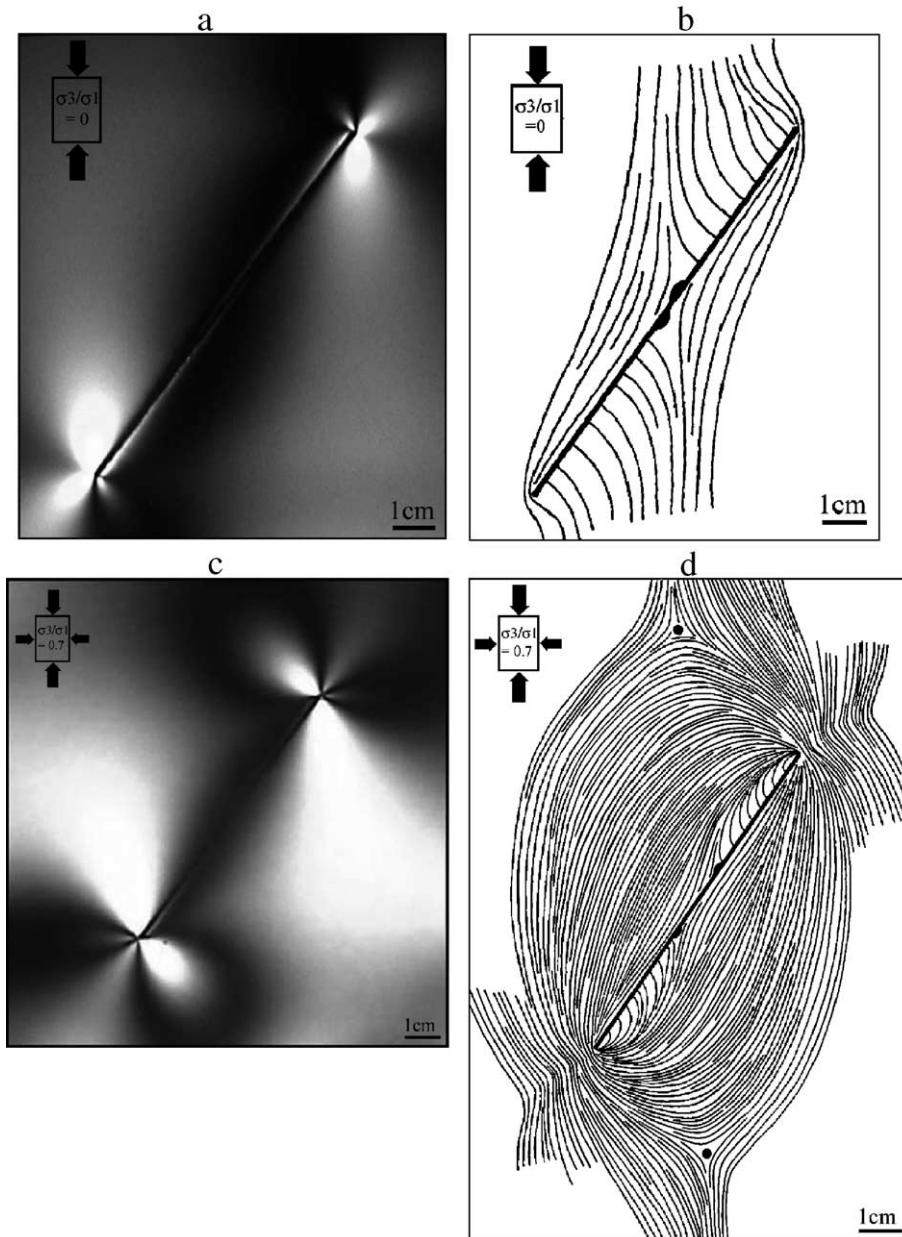


Fig. 9. (a) Photograph of isoclinics 30° around an oblique isolated defect during a photoelastic experiment where σ_3/σ_1 is 0. (b) Corresponding σ_{1L} trajectories. (c) Photograph of isoclinics 30° around the same oblique isolated fault during a photoelastic experiment where σ_3/σ_1 is 0.7. (d) Corresponding σ_{1L} trajectories. In a, b, c and d only the central visible part of the sample is presented (the upper and lower limits are not those of the plates), and black points on the figures are isotropic points.

4. Results

Given the geometry of the experimental device, the upper and lower parts of the plates could not be observed. That is why the stress trajectories presented above are not always perpendicular to the vertical limits of the figures, which are not those of the plates.

We first present results concerning the effect of increasing biaxial compressive load on stress trajectories around an isolated open defect. Fig. 6a to e are photographs of isoclinics 0° around the defect for σ_3/σ_1 equal to 0, 0.2, 0.4, 0.6 and 0.8, respectively. It was observed that the corresponding isoclinics were increasingly close to the defect walls with increasing biaxial compressive load. The same effect was observed for other orientations of the polarizers. Fig. 7a to e show σ_{1L} ($\sigma_{1L} = \sigma_1$ local) trajectories on one side of the defect, the other side being symmetrical with respect to the centre of the defect. A significant change in stress trajectory geometry was observed between the experiments with σ_3/σ_1 ratio evolving from 0.2 to 0.4. For low σ_3/σ_1 values (Fig. 7a and b), at the contact with the defect, the stress trajectories were perpendicular and parallel to the walls on each side of an isotropic point located along the defect. When σ_3/σ_1 was 0.4 (Fig. 7c), an isotropic point remained along the defect, but a new external isotropic point appeared away from the defect towards its tip, resulting in a complete reorganization of stress trajectories at the tip of the defect. These stress trajectories tended to loop along the defect segment facing the external isotropic point and between the defect tip and the isotropic point touching the defect. Fig. 8 gives the detailed geometry of isoclinics and corresponding σ_{1L} trajectories around an external isotropic point. At these points, the isoclinics of all orientations intersect (Fig. 8a). To ensure the coherency of trajectories away from and around the isotropic point, the only way to trace the trajectories is to make them diverge around it except for one of them, as shown in Fig. 8c. This kind of isotropic point is sometimes called a repulsive point (Vishay-micromesures, 1984).

As for the drastic change of stress trajectories when σ_3/σ_1 increased from 0.2 to 0.4, this result is consistent with Barquins and Petit (1992) who showed analytically that the stress trajectory stemming from the point of maximum tensile stress at the tip of

an open elliptical defect was completely modified and tended to loop along the fault edge for $0.236 < \sigma_3/\sigma_1 < 0.237$, together with some preliminary photoelastic trajectories drawn by Auzias (1995).

We also observed that when σ_3/σ_1 increased above 0.4 (Fig. 7d and e), the external isotropic point tended

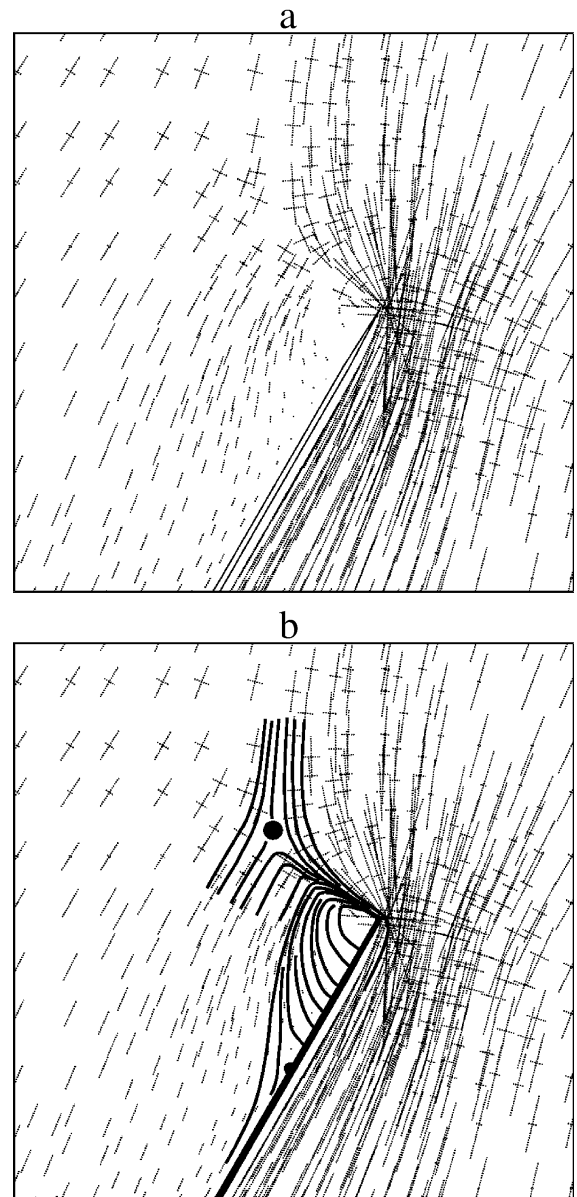


Fig. 10. (a) σ_{1L} and σ_{3L} trajectories around the tip of an open defect in a numerical experiment where σ_3/σ_1 is 0.7. (b) Interpreted σ_{1L} trajectories.

to move away from the fault tip, and towards the edges of the models where the main load was applied, the stress trajectory geometry remaining the same.

The drastic changes between the uniaxial and biaxial situations are shown in Fig. 9 which presents photographs of isoclinics 30° around an open elliptical fault

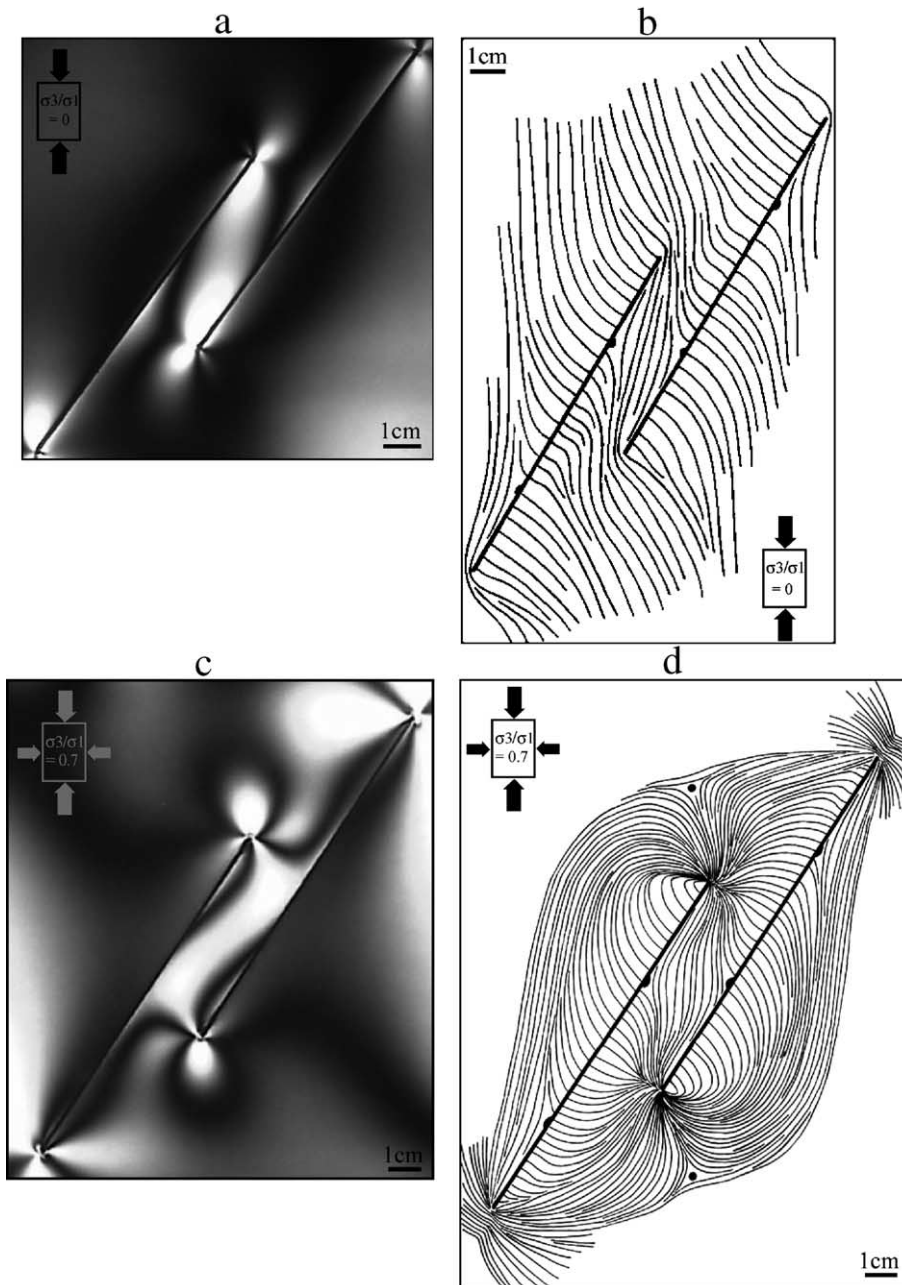


Fig. 11. (a) Photograph of isoclinics 30° within and around a compressive jog during a photoelastic experiment where σ_3/σ_1 is 0. (b) Corresponding σ_{1L} trajectories. (c) Photograph of isoclinics 30° within and around the same compressive jog during a photoelastic experiment where σ_3/σ_1 is 0.7. (d) Corresponding σ_{1L} trajectories.

and the corresponding σ_{1L} trajectories both for $\sigma_3/\sigma_1=0$ (Fig. 9a and b) and for $\sigma_3/\sigma_1=0.7$ (Fig. 9c and d). Other experiments have shown that the change in stress trajectories distribution is still observed for fault loading axis angle up to 60° . Fig. 10 presents stress trajectories (σ_1 and σ_3) around the tip of a defect submitted to biaxial load ($\sigma_3/\sigma_1=0.7$) derived from a numerical experiment. It clearly illustrates the superiority of the photoelastic method in terms of detailed study of stress trajectories. In effect, the numerical stress trajectories (Fig. 10a) were not clear: the isotropic points (external and located on the defect) were difficult to detect, and the fact that the σ_1 trajectories stemming from the points of maximum tensile stress at the tip of the defect tend to loop along the fault edge was not obvious. After interpretation (Fig. 10b), these characteristics were highlighted but as the numerical method did not permit to precise the location of the isotropic points, it would have been impossible to observe the changes in stress trajectories which were due to an increasing biaxial load ratio. The numerical method can produce reliable stress trajectories far from the defects, but close to them, imprecisions and anomalies are frequent (see stress trajectories in Bourne and Willemse, 2001).

In order to explore a more practical geological situation than the oblique isolated defect, we studied the stress trajectories around compressive and dilational jogs under biaxial compressive load, with $\sigma_3/\sigma_1=0.7$. In the following, the overlapping tips of defects are the tips involved in the overlapping zone, and the external tips of the defects are the other tips, which are not involved in the overlapping zone.

Fig. 11 presents photographs of isoclinics 30° around a compressive jog and the corresponding σ_{1L} trajectories both for $\sigma_3/\sigma_1=0$ (Fig. 11a and b) and for $\sigma_3/\sigma_1=0.7$ (Fig. 11c and d). The differences between the two loading situations had similar characteristics as in Fig. 9 (i.e. external isotropic points and looping trajectories). However, a new interesting stress trajectory geometry was observed. The overlapping tips of the defects were shown to be zones of high convergence of stress trajectories. Fig. 12 shows the details of isoclinics (Fig. 12a), the deduced crosses corresponding to two local principal stress orientations (Fig. 12b), and the corresponding stress trajectories (Fig. 12c) illustrating this stress trajectory geometry. Finally, Fig. 11b and d shows that both in the uniaxial

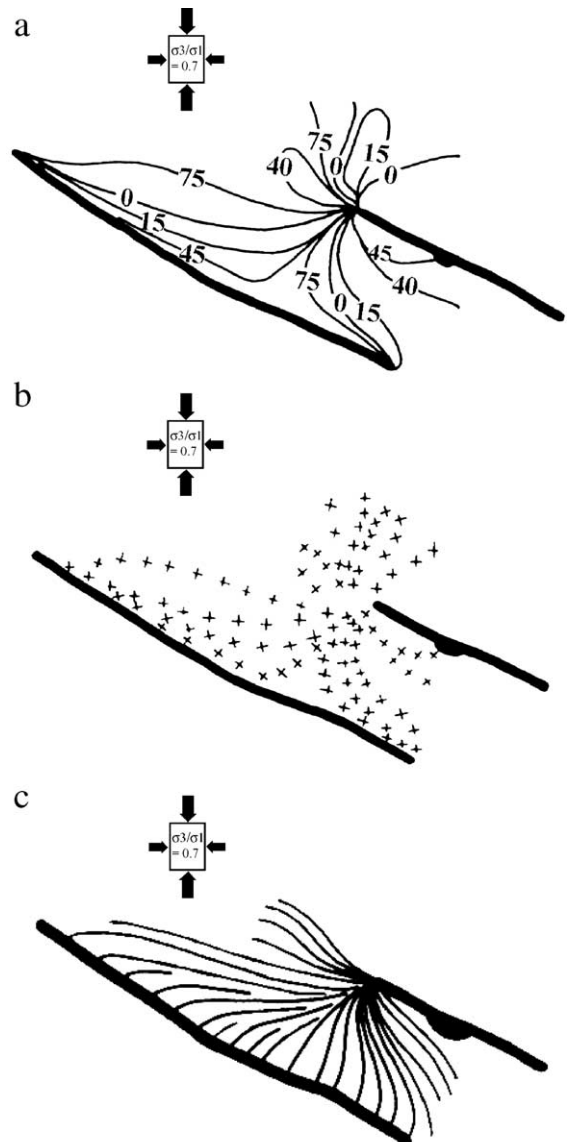


Fig. 12. Isoclinics (a), stress orientations (b) and σ_{1L} trajectories (c) corresponding to a characteristic biaxial geometry: convergence of σ_{1L} trajectories towards the tip of a fault in a complex compressive jog.

and biaxial cases, the main principal stress trajectories were either slightly oblique or perpendicular to the defect walls in the overlapping zone; this agrees with Auzias (1995).

Fig. 13 presents photographs of isoclinics 30° around dilational jog and the corresponding σ_{1L}

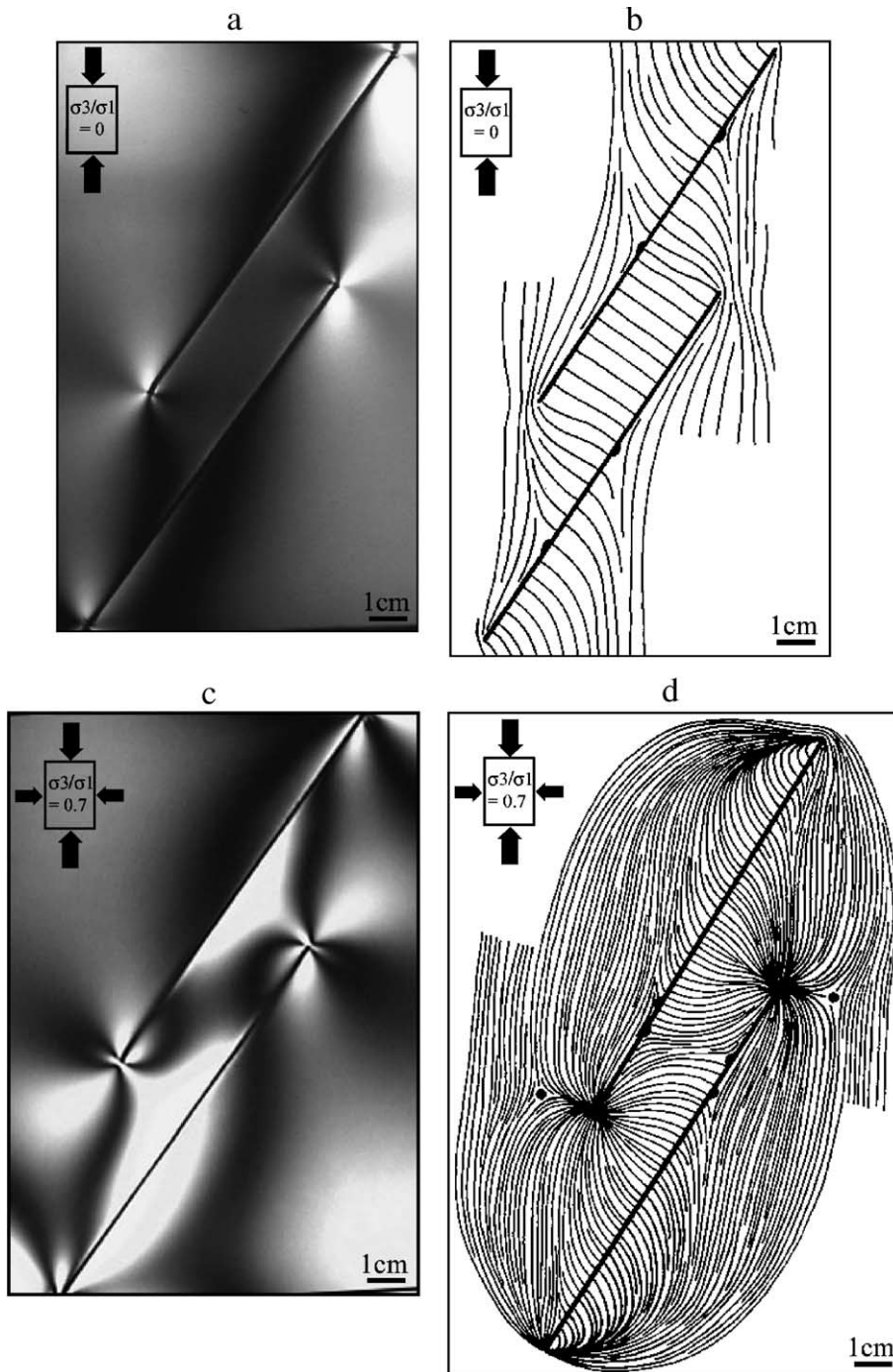


Fig. 13. (a) Photograph of isoclinics 30° within and around a dilational jog during a photoelastic experiment where σ_3/σ_1 is 0. (b) Corresponding σ_{1L} trajectories. (c) Photograph of isoclinics 30° within and around the same dilational jog during a photoelastic experiment where σ_3/σ_1 is 0.7. (d) Corresponding σ_{1L} trajectories.

trajectories both for $\sigma_3/\sigma_1=0$ (Fig. 13a and b) and for $\sigma_3/\sigma_1=0.7$ (Fig. 13c and d). The stress trajectories observed in this case were similar to those related to the compressive jog: the overlapping tips of the defects were shown to be zones of high convergence of stress trajectories. In this case, the uniaxial and the

biaxial situations led to different trajectories in the jog zone: under a uniaxial compressive load, stress trajectories were perpendicular to the defect walls, and under a biaxial compressive load, they were attracted by the two defect tips. In all the experiments presented, external isotropic points near the tips of the

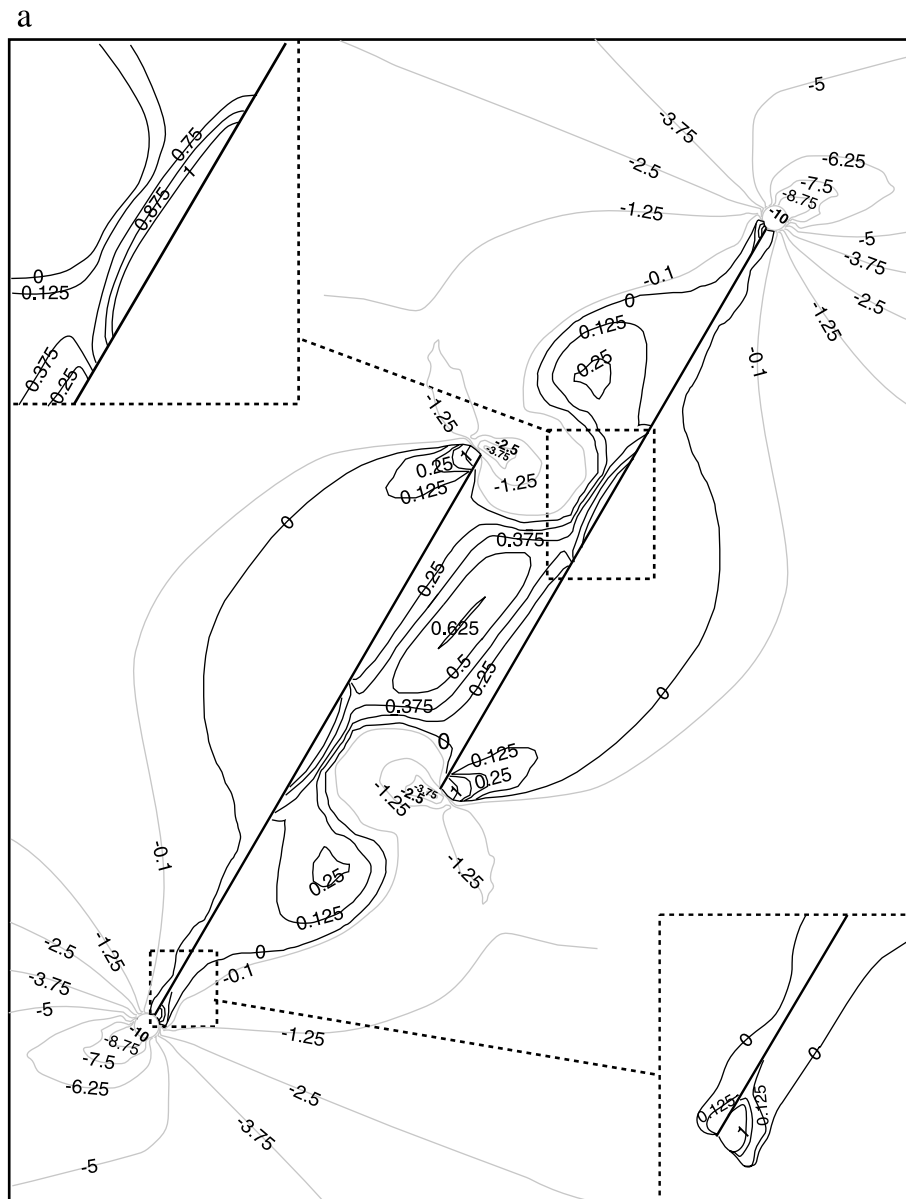


Fig. 14. Stress contours (MPa) derived from numerical experiments where σ_3/σ_1 is 0.7 (negative stress values correspond to compressive stress, and positive stress values correspond to tensile stress): (a) σ_{3L} contours within and around a compressive jog; (b) σ_{1L} contours within and around a compressive jog; (c) σ_{3L} contours within and around a dilational jog; (d) σ_{1L} contours within and around a dilational jog.

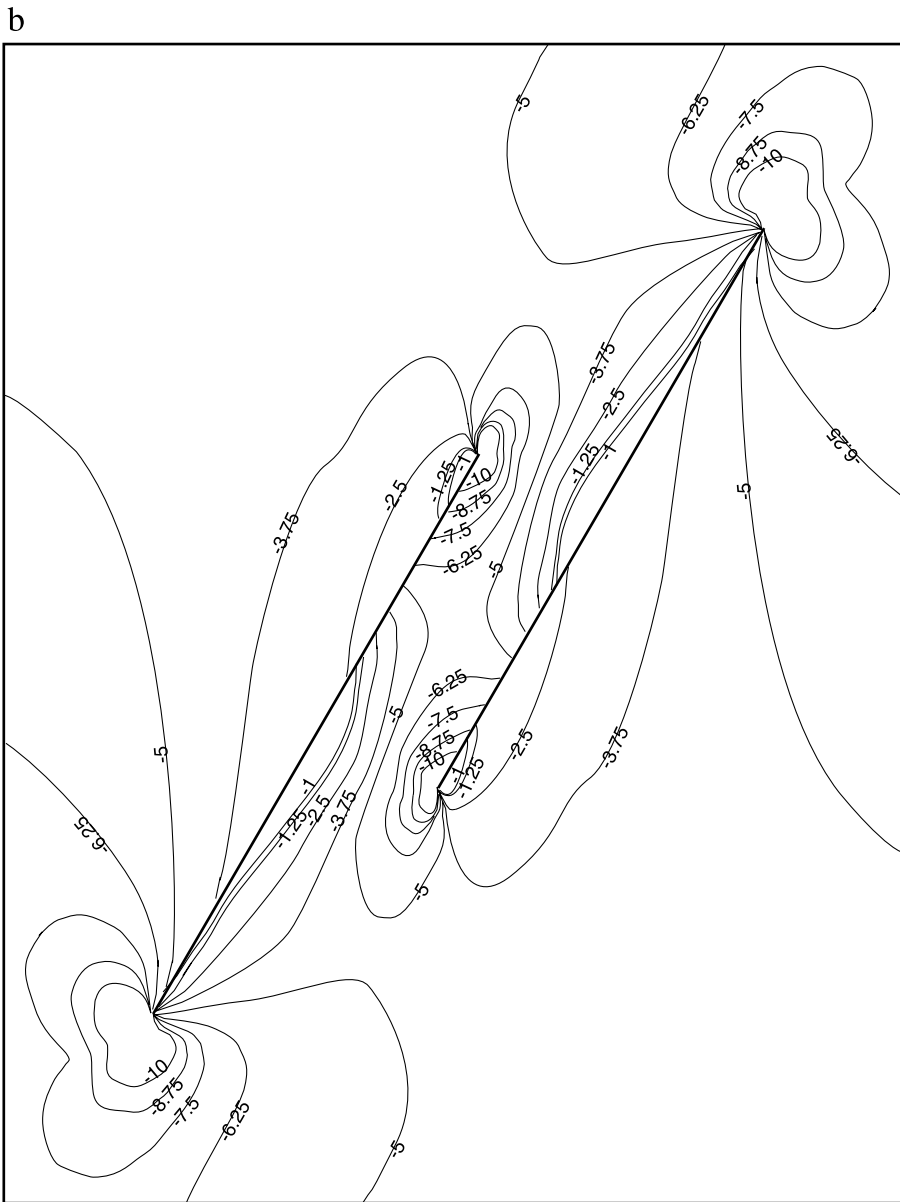


Fig. 14 (continued).

defects were observed. In the case of jogs, in addition to these external isotropic points, the convergence of stress trajectories towards the tips of overlapping defects was commonly observed.

Fig. 14 presents stress (σ_1 and σ_3) contours within and around compressive and dilational jogs, derived from numerical experiments. A first interesting obser-

vation in Fig. 14a and c is that, even under biaxial compressive load, σ_3 was a tensile stress in the intra-jog region for both compressive and dilational jogs, its intensity and distribution being very similar in both cases. The maximum σ_3 intensities (tensile stress) were located at the limits of the overlapping zone, close to the wall of a jog-defining fault, and facing the

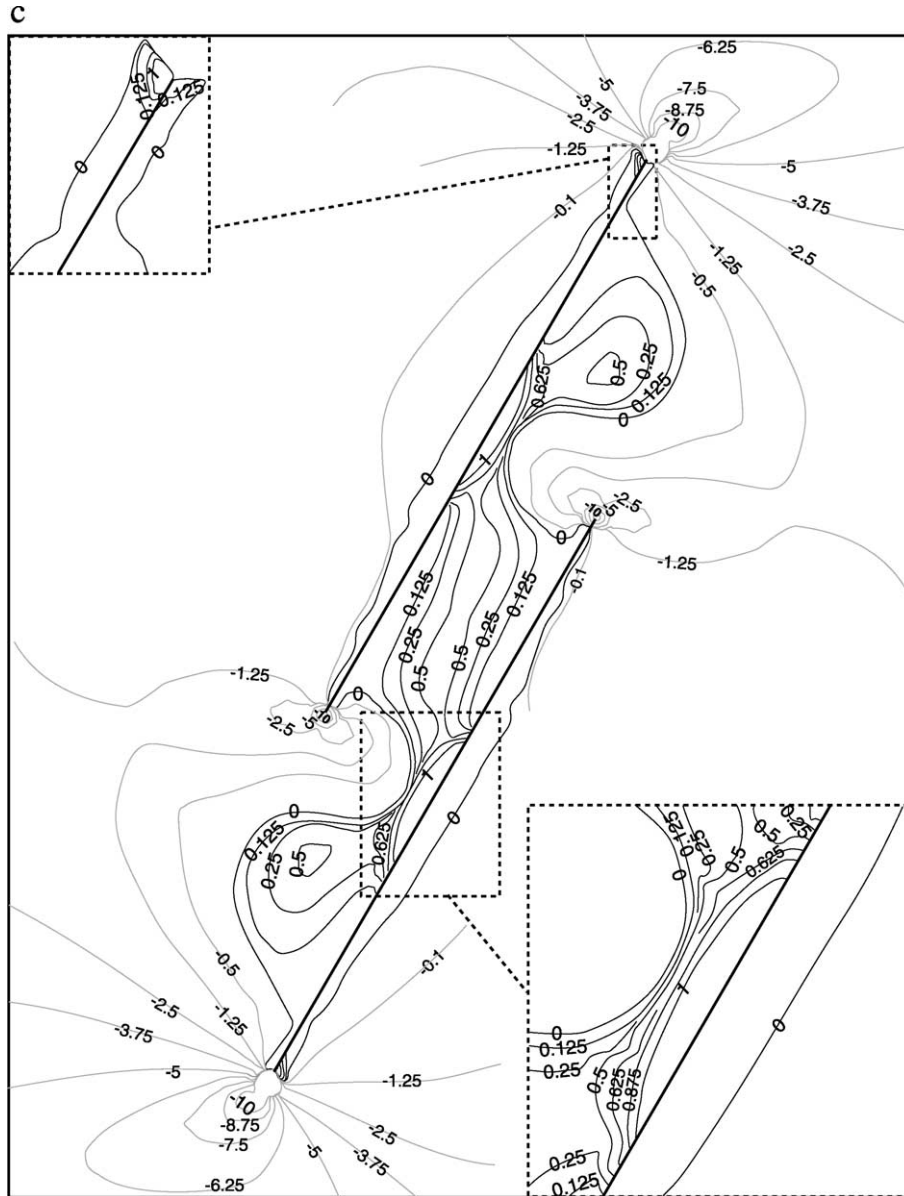


Fig. 14 (continued).

tip of the other jog-defining fault. Other high σ_3 intensities (tensile stress) were found near the overlapping tips of the defects, but on the external side. The minimum σ_3 intensities, corresponding to compressive stress, were found near the tips of the faults, and were 10 times stronger than the maximum tensile stress intensities in absolute value (-10 MPa vs. 1

MPa). Fig. 14b and d shows once again similar stress contours for both compressive and dilational jogs, in the case of σ_1 (all compressive stress). Here the maximum σ_1 intensities (i.e. the most compressive values of σ_1) were located near the tips of the defects, and other high σ_1 intensities were found in the centre of the intrajog region. Moreover, the minimum σ_1

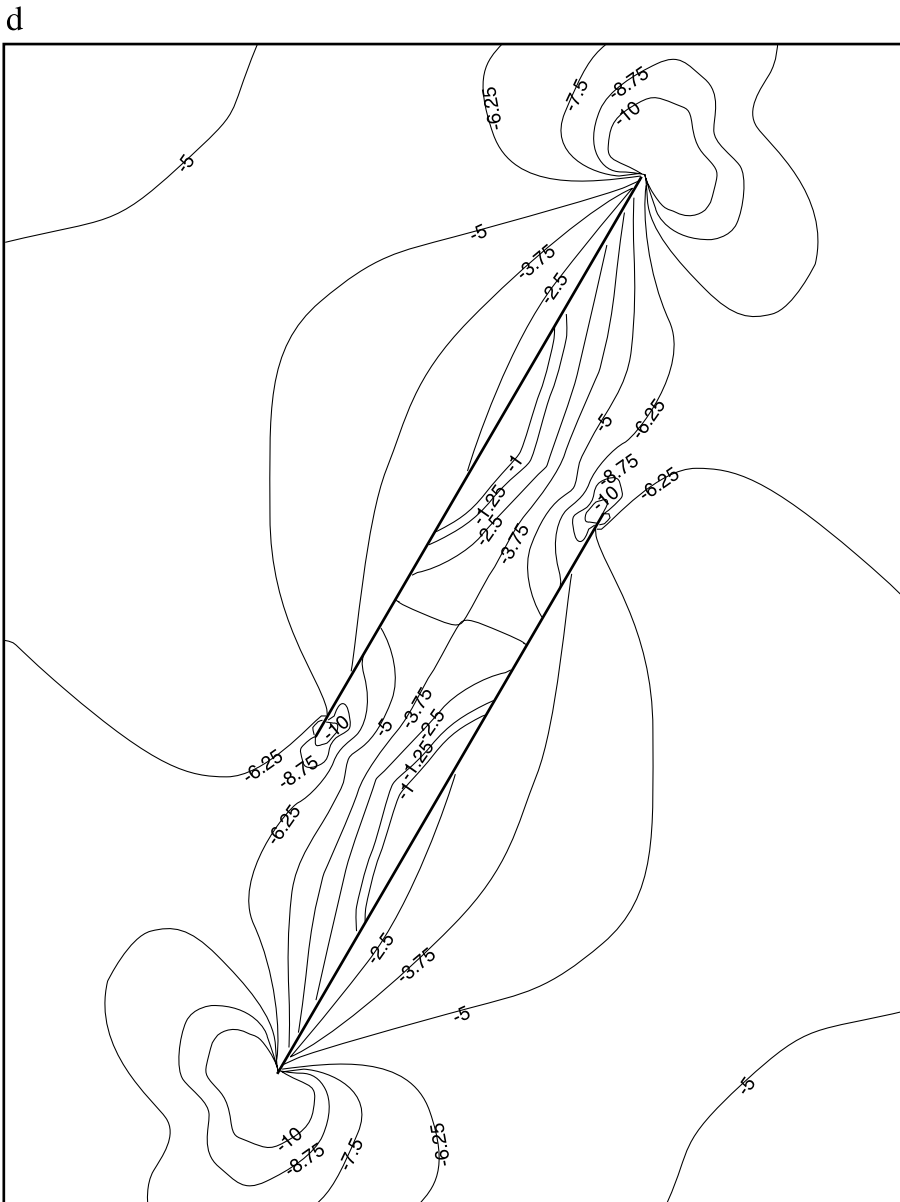


Fig. 14 (continued).

intensities (i.e. the less compressive values of σ_1) coincided with maximum σ_3 intensities (tensile stress) at the limits of the intrajog region, even if areas of minimum σ_1 were larger than areas of maximum σ_3 .

We also performed some preliminary analogue experiments on stress distributions around complex fault patterns inspired from fault patterns in a reser-

voir. An interesting observation illustrated by Figs. 15–17 is the presence of numerous isotropic zones (noted I). These zones were shown to be exclusively located in the acute angle between branching defects strongly oblique to the main loading axis, both for uniaxial and biaxial compressive loads (Figs. 15a,b, 16a,b and 17a,b, respectively). These figures show

that biaxial compressive load seemed to have little influence on the occurrence and distribution of such isotropic zones.

5. Interpretation

We observed that the stress trajectories were drastically modified by adding a lateral pressure up to 0.2

σ_1 in the experiments. These modifications can mainly be interpreted as the consequence of the occurrence of repulsive isotropic points away from the defects. The occurrence of these points can be related to the fact that when a lateral pressure is added, the minor local principal stress σ_{3L} tends to increase, leading to an increasing probability of getting σ_{3L} equal to σ_{1L} .

The similarity between the stress trajectory patterns and stress distributions within compressive and

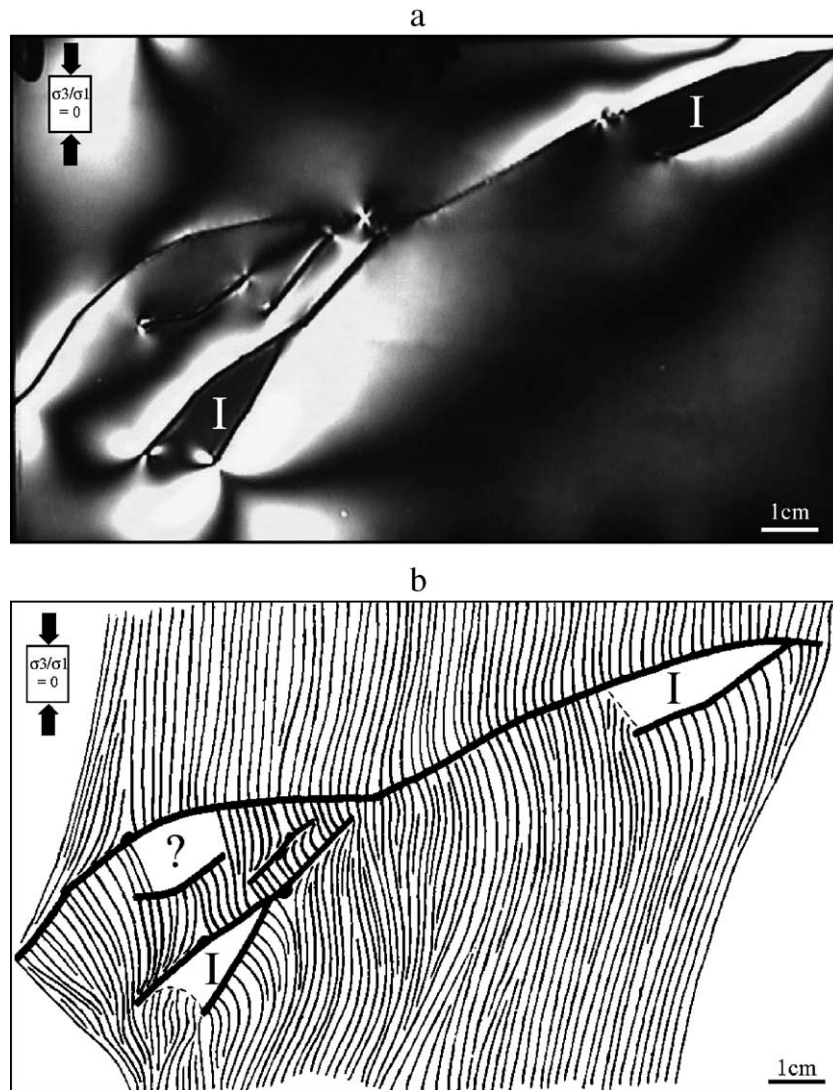


Fig. 15. (a) Photograph of isoclinics 0° around a complex fault pattern during a photoelastic experiment where σ_3/σ_1 is 0. Black zones between the branching faults are isotropic zones (I on the figure). (b) Corresponding σ_{1L} trajectories.

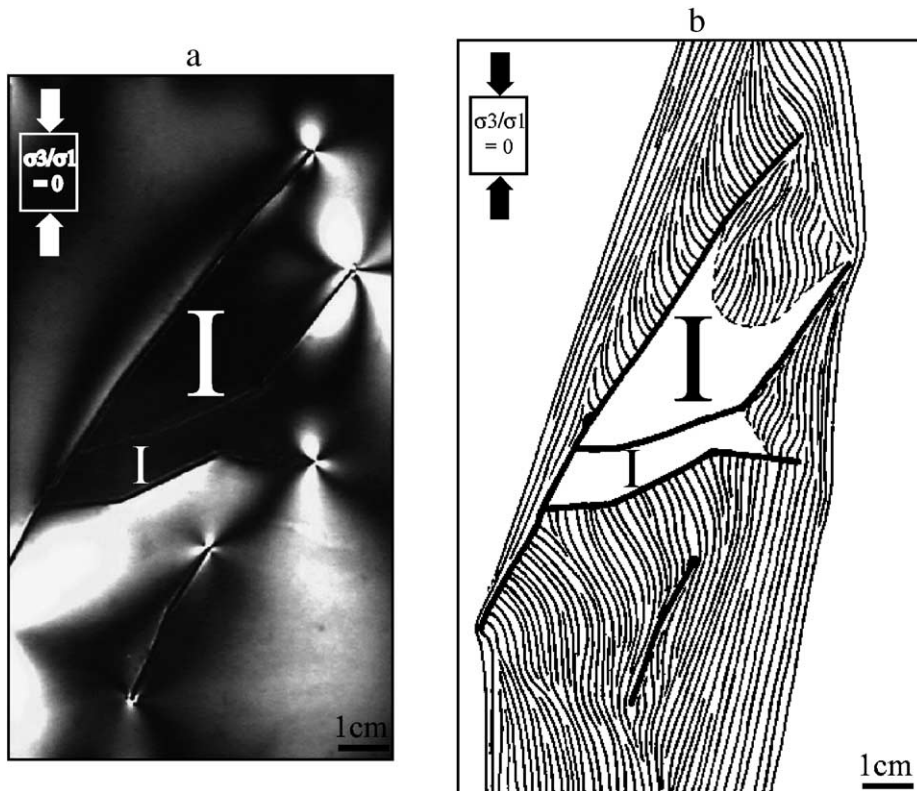


Fig. 16. (a) Photograph of isoclinics 0° around a complex fault pattern during a photoelastic experiment where σ_3/σ_1 is 0. Black zones between the branching faults are isotropic zones (I on the figure). (b) Corresponding σ_{1L} trajectories.

dilational jogs under biaxial compressive load conditions has been shown; it is very different from the uniaxial case shown in Figs. 11b and 13b. This observation can be explained as follows. In the uniaxial case, the shear displacement along the overlapping defects is important because they are well oriented (30°) and because the displacement is not limited by a lateral stress. The situations within the jog zones are well known to be strong tensile stress perpendicular to σ_{HL} trajectories (σ_{1L} and σ_{3L} in the experiments can be compared to σ_{HL} and σ_{hL} in geological contexts) in the dilational jog and strong compression parallel to σ_{HL} trajectories in the compressive jog. However, if a significant lateral pressure is applied ($0.7\sigma_1$ in the experiments), it strongly inhibits the shear displacement along the overlapping faults. This results in the far less contrasted stress situations observed in the overlapping zones, illustrated by Figs. 11d and 13d (stress trajectories), and

by Fig. 14 (stress contours): stress trajectories and stress contours are very similar in both dilational and compressive jogs under biaxial compressive load, which was not the case under uniaxial compressive load.

In complex geometries, the only slight influence of biaxial compared with uniaxial compressive load on isotropic zones distribution has to be interpreted. These isotropic zones were only observed at the acute angle between branching defects with high obliquity to the major applied compression. In fact, they are “protected” zones, i.e. zones where the stress is not transmitted because the faults are open. In such a situation, adding a lateral pressure would not modify their distribution. This conclusion is valid if the zones are surrounded by frictionless defects, the difference between this situation (frictionless defects) and the experimental situation (open defects) being that the stress is nil in the

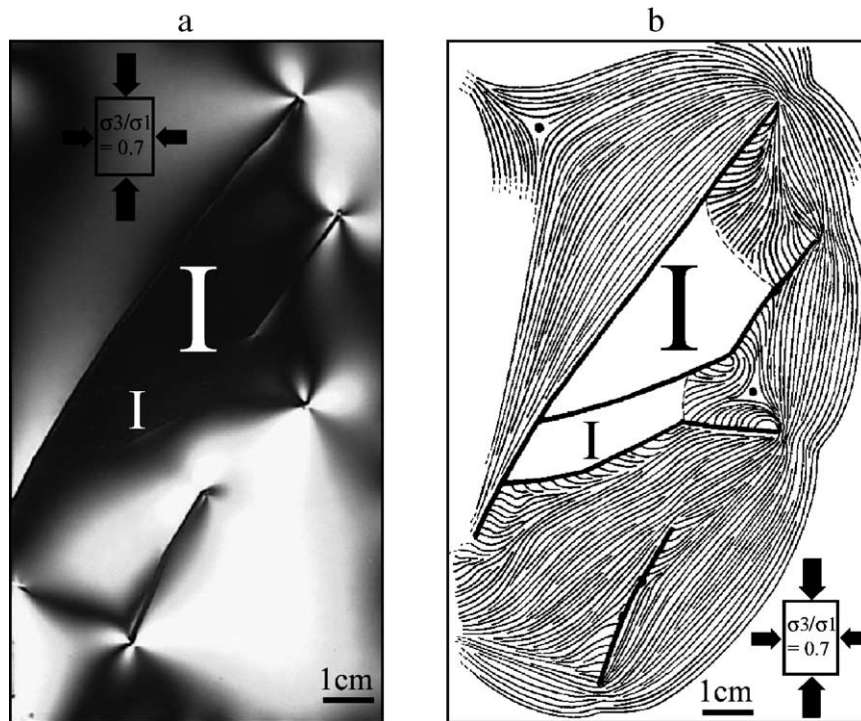


Fig. 17. (a) Photograph of isoclinics 0° around the complex fault pattern presented in Fig. 12, but during a photoelastic experiment where σ_3/σ_1 is 0.7. Black zones between the branching faults are isotropic zones (I on the figure). (b) Corresponding σ_{3L} trajectories.

latter case, whereas it is isotropic in the former case.

6. Discussion

We examine here some implications of our results on fracture behaviour and hydrodynamics at depth in high biaxial compressive load ratios. Firstly, joints, which are markers of σ_H paleostress field trajectories (Rawnsley et al., 1992, 1997; Auzias et al., 1997; Engelder and Geiser, 1980), never exhibit the patterns suggested by our trajectories, especially around faults. A general explanation is that high horizontal compression ratios do not encourage the formation of joint sets. However, the biaxial local compressive state could favour the shear reactivation of pre-existing joints or faults oriented at a suitable angle with respect to σ_{HL} . Thus, fluid flow at depth in oil reservoirs could be indirectly influenced by the stress contours and the geometry of stress trajectories described above. Fol-

lowing the approach of Connolly and Cosgrove (1999a), we may suppose that the fluid flow is controlled by the distribution of areas of high and low mean stress within the jogs, i.e. that fluid migration may occur in response to mean stress gradients induced by the tectonic loading (Oliver, 1986). This may permit to discuss possible flows within our jog models, even if actually, fluid migration should also be controlled by complex factors such as the characteristics of faults and fractures (orientation with the local stress, presence of gouge or mineral filling, etc.), or the existing hydraulic gradient and permeability anisotropy due to layering (Sibson, 1996), which cannot be considered in the present study.

The distribution differential stress within the jog models is also very important, because high differential stress may enhance fracture reactivation, and reactivated fractures are often very conductive (Sibson, 2000).

Fig. 18 presents in a simplified way the main tendencies in terms of mean stress (Fig. 18a) and

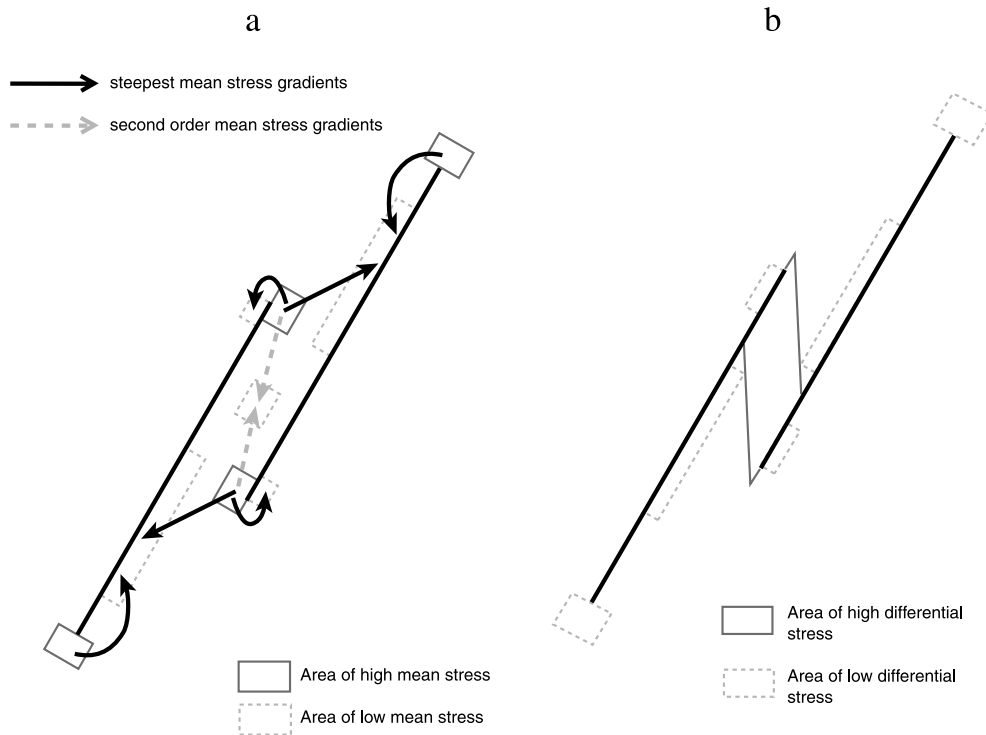


Fig. 18. (a) Simplified map of high and low mean stress areas within and around a compressive jog. (b) Simplified map of high and low differential stress areas within and around a compressive jog.

differential stress (Fig. 18b) within and around the compressive jog, derived from Fig. 14a and b. The areas of high mean stress (Fig. 18a) are exclusively located at the tips of the jog defining faults. No high mean stress are found far from the intrajog region. The areas of low mean stress exactly coincide with the areas of maximum tensile stress (σ_3) and minimum compressive stress (σ_1) shown in Fig. 14a and b. These zones are located close to a jog-defining fault and facing the overlapping tip of the other jog-defining fault at the limits of the intrajog region. Other zones of low mean stress are found near the overlapping tips of the defects on the external edge of the faults, and in the centre of the intrajog region. Therefore, the mean stress gradients are steepest between the tips of the faults (areas of high mean stress) and the areas located along the wall of a fault, and facing the overlapping tip of the other fault (black arrows). Other high mean stress gradients exist between the overlapping tips of faults and areas located near them, but on the external edge of the faults. Second-order

mean stress gradients exist between the overlapping tips of faults and the centre of the intrajog region (dashed arrows), suggesting possible flow directions within the compressive jog.

Fig. 18b shows that the area of high differential stress is in the centre of the intrajog region, between the overlapping tips of faults. Areas of low differential stress coincide with areas of low mean stress at the limits of the intrajog region, but low differential stress areas are also found near the tips of the defects. Consequently, the most favourable area in terms of fracture reactivation in the compressive jog (presenting both high differential stress and low mean stress) is the centre of the intrajog region. This area is expected to be an area towards which fluids may migrate (and where fluids may accumulate), and fracture reactivation may help such migration.

Fig. 19 presents in a simplified way the main tendencies in terms of mean stress (Fig. 19a) and differential stress (Fig. 19b) within and around the dilational jog, derived from Fig. 14c and d. Once

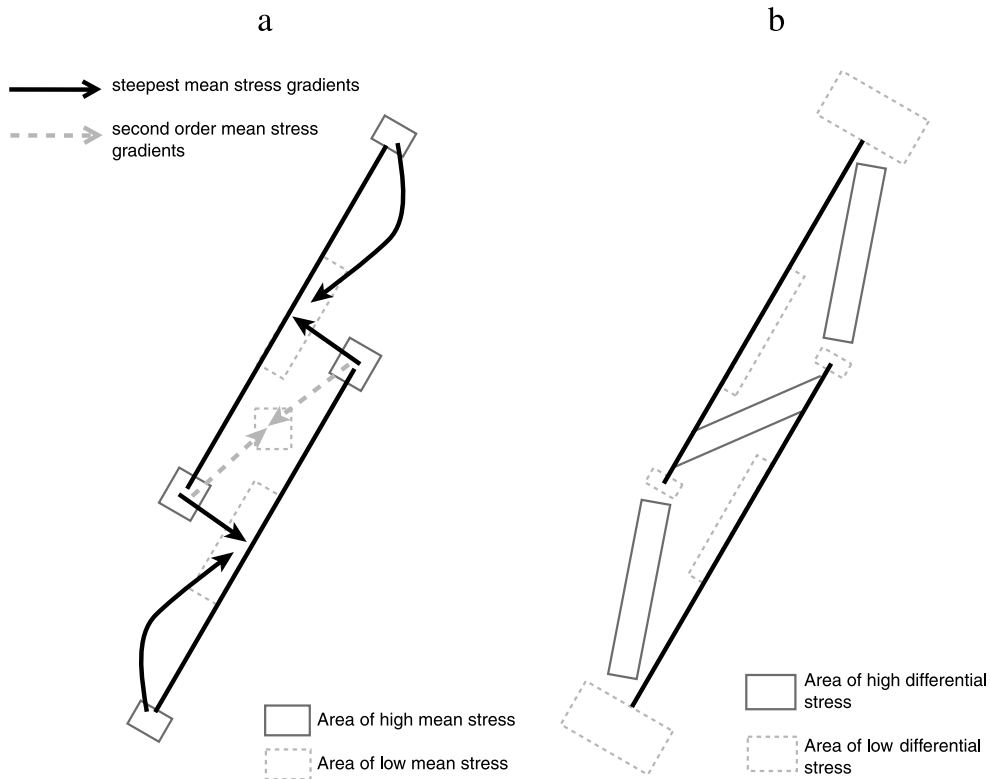


Fig. 19. (a) Simplified map of high and low mean stress areas within and around a dilational jog. (b) Simplified map of high and low differential stress areas within and around a dilational jog.

again, areas of high mean stress (Fig. 19a) are exclusively located at the tips of the jog-defining faults. The areas of low mean stress exactly coincide with areas of maximum tensile stress (σ_3) and minimum compressive stress (σ_1) shown in Fig. 14b and d. These zones are located close to a jog-defining fault and facing the overlapping tip of the other fault. The centre of the intrajog region also proves to be a zone of moderate mean stress. The mean stress gradients are steepest between the zones of high mean stress (tips of faults) and the areas located close to a jog-defining fault and facing the overlapping tip of the other jog-defining fault (black arrows). Second-order mean stress gradients exist between the overlapping tips of faults and the centre of the intrajog region (dashed arrows), suggesting possible flow directions within the dilational jog. Fig. 19b shows that the areas of high differential stress are located at the limits of the region delimited by the faults, and between the

overlapping tips of the defects, in the intrajog region. Areas of low differential stress coincide with areas of low mean stress, and are also found at the tips of the jog-defining faults. As it was observed in the case of the compressive jog, the centre of the intrajog region is expected to be both an area towards which fluid may migrate (and where fluid may accumulate), and a favourable area in terms of fracture reactivation. Concerning the isotropic zones shown in the photoelastic models, i.e. zones where the differential stress is nil, fracture behaviour is only controlled by normal stress. The described isotropic points correspond to the repulsive situation where trajectories tend to diverge. That means that σ_{1L} must diminish towards these points corresponding to a zone around the point where the differential stress is diminished and therefore unfavourable to reactivation (see the classical relationship between stress intensity and trajectories convergence in Vishay-micromesures, 1984). This is

confirmed by numerical stress contours shown in Fig. 14b and d, which indicate that the intensity of σ_{IL} diminish towards the isotropic points. The isotropic points attached to the fault walls correspond to a diverging situation, too, and thus to unfavourable conditions for reactivation.

Finally, in biaxial compressive load conditions, one can wonder if some mode I tensile rupture would be possible at fault tip. Barquins et al. (1991) have shown, using a mathematical model describing the tensile stress distribution at the tip of an open elliptical crack of various angles under various biaxial compressive loads, that even for very high biaxial stress ratios, tensile stress which may trigger mode I rupture is still present at fault tip provided the angle of the fault with respect to the main load is high. That would mean that mode I rupture could occur as branched fractures located at the tips of high angle faults under high biaxial stress ratios.

7. Conclusion

The main results are as follows. Firstly, biaxial compressive load drastically modified the stress trajectories around fault models for ratios σ_3/σ_1 up to 0.2: stress trajectories became circular at the defect tips, and mainly parallel to the defect away from it. These modifications of stress trajectories with biaxial compressive load were mainly controlled by the appearance of external isotropic points located near the tips, around where trajectories diverged. These points tended to move away from the tips towards the direction of the main load direction with increasing biaxial compressive load. The described isotropic points (touching the defects and away from them) delimited zones strongly unfavourable to shear reactivation.

Secondly, in the case of biaxial compressive load, stress trajectories and contours within compressive and dilational jogs proved to be relatively similar, although the corresponding uniaxial situations are very different. We suggest that such similar behaviours of jogs with biaxial compressive load are due to the fact that lateral pressure inhibits the shear displacement along the overlapping faults, leading to far less contrasted stress situations in jogs under biaxial compressive load than under uniaxial compressive load.

Thirdly, under biaxial compressive load, for both two jog types, the centre of the overlapping zone proved to be an area towards which fluids may migrate from the tips of the faults in response to mean stress gradients, and a favourable area in terms of fracture reactivation, which may help fluid transfer and storage. Fluids may also migrate towards areas located along a jog-defining fault and facing the overlapping tip of the second jog-defining fault.

Fourthly, in the case of biaxial compressive load, the analysis of stress trajectories around compressive and dilational jogs and complex fault patterns showed that the overlapping tips of the defects are zones of high stress trajectory convergence.

Finally, some isotropic zones were described; they were shown to be exclusively localised in the acute angle between branching defects strongly oblique to the main load axis. In these “protected” zones, which are not strongly influenced by biaxial compressive load, fracture behaviour is only controlled by normal stress.

Acknowledgements

This study has been carried out with the financial support of TotalFinaElf. We thank Mark Jessell and the anonymous reviewer for comments and suggestions which have improved the quality of the paper. We are also grateful to Michel Barquins whose great experience of stress deviations around fault models and advice about the experiments were much appreciated. We thank Jean Chéry and Pascal Cortes for fruitful discussions and comments. Finally, many thanks to Cornell University and Cornell Fracture Group for free use of Franc2D.

References

- Auzias, V., 1995. Contribution à la caractérisation tectonique des réservoirs fracturés. PhD thesis, Université Montpellier II.
- Auzias, V., Rives, T., Rawnsley, K.D., Petit, J.P., 1997. Fracture orientation modelling in the vicinity of a horizontal well. Bulletin du Centre de Recherches Elf Exploration Production 21, 381–397.
- Barquins, M., Petit, J.P., 1992. Kinetic instabilities during the propagation of a branch crack: effects of loading conditions and internal pressure. *Journal of Structural Geology* 14, 893–903.

- Barquins, M., Petit, J.P., Maugis, D., Ghalayini, K., 1991. Path and kinetics of branching from faults under uniaxial and biaxial compressive loading. *International Journal of Fracture* 54, 139–163.
- Barker, D.B., Sanford, R.J., Chona, R., 1985. Determining K and related stress-field parameters from displacement fields. *Experimental Mechanics* 25, 399–406.
- Baumgärtner, J., Zoback, M.D., 1989. Interpretation of hydraulic pressure–time records using interactive analysis methods. *International Journal of Rock Mechanics and Mining Sciences* 26, 461–470.
- Bertoluzza, L., Perotti, C.R., 1997. A finite-element model of the stress field in strike–slip basins: implications for the Permian tectonics of the Southern Alps (Italy). *Tectonophysics* 280, 185–197.
- Bodin, P., Brown, S., Matheson, D., 1998. Laboratory observations of fault-normal vibrations during stick–slip. *Journal of Geophysical Research* 103, 29931–29944.
- Bouissou, S., Petit, J.P., Barquins, M., 1998a. Normal load, slip rate and roughness influence on the polymethylmethacrylate dynamics of sliding: 1. Stable sliding to stick–slip transition. *Wear* 214, 156–164.
- Bouissou, S., Petit, J.P., Barquins, M., 1998b. Normal load, slip rate and roughness influence on the polymethylmethacrylate dynamics of sliding: 2. Characterisation of the stick–slip phenomenon. *Wear* 215, 137–145.
- Bouissou, S., Petit, J.P., Barquins, M., 1998c. Experimental evidence of contact loss during stick–slip: possible implications for seismic behaviour. *Tectonophysics* 295, 341–350.
- Bourne, S.J., Willemse, E.J.M., 2001. Elastic stress control on the pattern of tensile fracturing around a small fault network at Nash Point, UK. *Journal of Structural Geology* 23, 1753–1770.
- Bourne, S.J., Rijkels, L., Stephenson, B.J., Willemse, E.J.M., 2001. Predictive modelling of naturally fractured reservoirs using geomechanics and flow simulation. *GeoArabia (Manama)* 6 (1), 27–42.
- Brown, S.R., 1987. Fluid flow through rock joints: the effect of surface roughness. *Journal of Geophysical Research* 92, 1337–1347.
- Connolly, P., Cosgrove, J., 1999a. Prediction of fracture-induced permeability and fluid flow in the crust using experimental stress data. *American Association of Petroleum Geologists Bulletin* 83 (5), 757–777.
- Connolly, P., Cosgrove, J., 1999b. Prediction of static and dynamic fluid pathways within and around dilational jogs. *Geological Society Special Publications* 155, 105–121.
- Dally, J.W., Sanford, R.J., 1978. Strain gage methods for measuring the opening-mode Stress Intensity Factor, K_I . *Experimental Mechanics* 18, 441–448.
- Dally, J.W., Sanford, R.J., 1987. Classification of Stress Intensity Factors from isochromatics fringe patterns. *Experimental Mechanics* 27, 381–387.
- de Jossineau, G., Bouissou, S., Petit, J.P., Barquins, M., 2001. Experimental analysis of slip distribution along a fault segment under stick–slip and stable sliding conditions. *Tectonophysics* 337, 85–98.
- Dholakia, S.K., Aydin, A., Pollard, D.D., Zoback, M.D., 1998. Fault-controlled hydrocarbon pathways in the Monterey Formation, California. *American Association of Petroleum Geologists Bulletin* 82, 1551–1574.
- Dieterich, J.H., Kilgore, B.D., 1994. Direct observation of friction contacts: new insights for state-dependent properties. *Pure and Applied Geophysics* 143, 283–302.
- Dieterich, J.H., Kilgore, B.D., 1996. Imaging surface contacts: power law contact distributions and contact stresses in quartz, calcite, glass and acrylic plastic. *Tectonophysics* 256, 219–239.
- Engelder, T., 1993. *Stress regimes in the lithosphere*. Princeton Univ. Press, Princeton, New Jersey, USA.
- Engelder, T., Geiser, P., 1980. On the use of regional joint sets as trajectories of paleostress fields during the development of the Appalachian plateau, New York. *Journal of Geophysical Research* 85, 6319–6341.
- Evans, K., Engelder, T., Plumb, R.A., 1989. Appalachian Stress Study I: a detailed description of in situ stress variations in Devonian Shales of the Appalachian Plateau. *Journal of Geophysical Research* 94, 7129–7154.
- Feng, Z., Rowlands, R.E., Sanford, R.J., 1991. Stress intensity determination by an experimental–numerical hybrid technique. *Journal of Strain Analysis for Engineering Design* 26, 243–251.
- Haimson, B.C., Doe, T.W., 1983. State of stress, permeability, and fractures in the Precambrian granite of northern Illinois. *Journal of Geophysical Research* 88, 7355–7372.
- Haimson, B.C., Rummel, F., 1982. Hydrofracturing stress measurements in the Iceland Research Drilling Project drill hole at Reydarfjörður, Iceland. *Journal of Geophysical Research* 87, 6631–6659.
- Hetényi, M., 1966. *Handbook of experimental stress analysis*. Wiley, New York.
- Hyett, A.J., Hudson, J.A., 1990. A photoelastic investigation of the stress state close to rock joints. In: Barton, N.R., Stephansson, O. (Eds.), *Rocks joints*. Balkema, Rotterdam, pp. 227–233.
- Kattenhorn, S.A., Pollard, D.D., 2001. Integrating 3-D seismic data, field analogs and mechanical models in the analysis of segmented normal faults in the Wytch Farm oil field, southern England, United Kingdom. *American Association of Petroleum Geologists Bulletin* 85, 1183–1210.
- Kattenhorn, S.A., Aydin, A., Pollard, D.D., 2000. Joints at high angles to normal fault strike: an explanation using 3-D numerical models of fault-perturbed stress fields. *Journal of Structural Geology* 22, 1–23.
- Maerten, L., Gillespie, P., Pollard, D.D., 2002. Effects of local stress perturbation on secondary normal fault development. *Journal of Structural Geology* 24, 145–153.
- Nemat-Nasser, S., Horii, H., 1982. Compression induced non planar crack extension with application to splitting, exfoliation and rock-burst. *Journal of Geophysical Research* 87, 6805–6821.
- Oliver, J., 1986. Fluids expelled tectonically from orogenic belts: their role in hydrocarbon migration and other geologic phenomena. *Geology* 14, 99–102.
- Petit, J.P., Barquins, M., 1987. Formation de fissures en milieu confiné dans le PMMA (polyméthacrylate de méthyle): modèle analogique de structures tectoniques cassantes. *Comptes Rendus de l'Académie des Sciences de Paris, série IIB* 324, 299–306.

- Rawnsley, K.D., Rives, T., Petit, J.P., Hencher, S.R., Lumsden, A.C., 1992. Joint development in perturbed stress fields near faults. *Journal of Structural Geology* 14, 939–951.
- Rawnsley, K., Auzias, V., Petit, J.P., Rives, T., 1997. Extrapolating fracture orientations from horizontal wells using stress trajectory models. *Petroleum Geoscience* 3, 145–152.
- Sanford, R.J., 1989. Determining fracture parameters with full field optical methods. *Experimental Mechanics* 29, 241–247.
- Segall, P., Pollard, D.D., 1980. Mechanics of discontinuous faults. *Journal of Geophysical Research* 85, 4337–4350.
- Sibson, R.H., 1996. Structural permeability of fluid-driven fault–fracture meshes. *Journal of Structural Geology* 18, 1031–1042.
- Sibson, R.H., 2000. Fluid involvement in normal faulting. *Journal of Geodynamics* 29, 469–499.
- Stock, J.M., Healy, J.H., 1988. Continuation of a deep borehole stress measurement profile near the San Andreas fault: 2. Hydraulic fracturing stress measurements at Black Butte, Mojave Desert, Ca. *Journal of Geophysical Research* 93, 15196–15206.
- Taylor, W.L., Pollard, D.D., Aydin, A., 1999. Fluid flow in discrete joint sets: field observations and numerical simulations. *Journal of Geophysical Research* 104, 28983–29006.
- Vishay-micromesures, 1984. *Encyclopédie d'analyse des contraintes*. Jean Avril, Malakoff, France.
- Wawrzynek, P.A., Ingraffea, A.R., 1987. Interactive finite element analysis of fracture processes: an integrated approach. *Theoretical and Applied Fracture Mechanics* 8, 137–150.
- Wu, F.T., Thomson, K.C., Kuenzler, H., 1972. Stick–slip propagation velocity and seismic source mechanism. *Bulletin of the Seismological Society of America* 62, 1621–1628.
- Zoback, M.D., Tsukahara, H., Hickman, S., 1980. Stress measurements at depth in the vicinity of the San Andreas fault. *Journal of Geophysical Research* 85, 6157–6173.